VI International Conference on Computational Methods in Marine Engineering
MARINE 2015
F. Salvatore, R. Broglia and R. Muscari (Eds)

NUMERICAL SIMULATION OF CAVITATING SHIP PROPELLER FLOW AND ASSESSMENT OF EROSION AGGRESSIVENESS

MARINE 2015

BERND BUDICH[*], **STEFFEN J. SCHMIDT**[*]
AND NIKOLAUS A. ADAMS[*]

[*]Institute of Aerodynamics and Fluid Mechanics (AER)
Technische Universität München
Boltzmannstr. 15, 85748 Garching b. München, Germany
e-mail: bernd.budich@tum.de, web page: http://www.aer.mw.tum.de

Key words: Numerical Simulation, Propeller Cavitation, Cavitation Erosion

Summary *Our contribution focuses on the evaluation of cavitation aggressiveness on the cavitating model propeller VP1304 by numerical simulation. To this respect, we employ a density-based, finite volume method, based on a barotropic, homogeneous mixture model. Fully accounting for two-phase compressibility, collapse-induced instantaneous peak pressures and associated wave dynamics are captured by the chosen approach.*

The maximum instantaneous pressures registered on material surfaces allow for a qualitative identification of erosion-sensitive areas. Furthermore, a collapse detection algorithm is applied for an automated recording of isolated cavity collapse events. Impact load spectra showing rate and intensity distributions of recorded collapses is utilized for a quantitative evaluation of cavitation aggressiveness. While the cavitating tip vortex is stable and does not lead to collapse events in the vicinity of the propeller, material erosion can be expected in the suction side root region due to a highly unsteady root cavitation.

1 INTRODUCTION

Cavitating flow is frequently encountered in naval and propulsor hydrodynamics. Propeller performance can be substantially deteriorated by cavitation. The collapse-like recondensation of vapor pockets results in the formation of intense shock waves. In addition to the generation of noise and structural vibrations, this constitutes a principal mechanism of material erosion. Cavitation thus limits the lifespan of affected components [1, 2] and causes increased cost for maintenance and overhaul. Predicting the expected material erosion hence is of particular interest for propeller design, necessitating an improved understanding of the underlying flow dynamics.

Numerical methods can provide important insights into propeller flow, where experimental investigations are often limited, e.g. for resolving internal flow structures within cavitating regions. Most state-of-the-art simulations are based on incompressibility assumptions. It is well-known, however, that shock waves are generated upon cavity collapse [3]. In order to accurately capture collapse mechanisms and collapse-induced pressure peaks, two-phase compressibility thus needs to be taken into account.

We therefore chose a density-based, fully compressible numerical method, employing a homogeneous mixture model. Collapse pressure peaks and induced acoustics are resolved and even complex flow configurations with a coexistence of various cavitation types are captured [4, 5]. Schmidt *et al.* [6] investigated the collapse of a cloud of bubbles and found that even in highly under-resolved cases, frequently encountered for the simulation of engineering-relevant systems, erosion-related quantities can be predicted nearly independent of the spatial resolution. Moreover, the method has been successfully applied by Mihatsch *et al.* [7] for the assessment of erosion aggressiveness. The authors show that collapse locations in the simulation agree with experimentally observed material erosion and agreement for the load spectra derived from experimental and numerical pressure sensors is achieved. In a recent publication [8], the authors further obtain accordance between experimental pitting rates and numerically predicted collapse rates.

Previously, we applied the approach to a cavitating model propeller, see Budich *et al.* [9]. Results have been validated with experimental and numerical studies of the same configuration. In the present contribution, we focus on the numerical quantification flow aggressiveness by evaluating the global and local collapse load spectra. To this respect, section 2 reviews the model assumptions and the chosen numerical approach. Two methods for the identification of erosion-sensitive areas are discussed. Subsequently, section 3 presents the selected test case together with the chosen computational setup. Results are analyzed in section 4. Finally, section 5 concludes with a summary of the findings and an outlook.

2 NUMERICAL APPROACH

2.1 Assumptions and Numerical Method

A short summary of model assumptions and the numerical method employed for the present study is included here for completeness. For more details, refer to Ref. [9].

We assume local mechanical and thermodynamic equilibrium for the two-phase flow of water and water vapor. Neglecting the influence of surface tension and interface slip, pressure and velocity at phase boundaries can be treated as continuous. Consequently, a homogeneous mixture approach is applied. We further assume barotropic flow and treat two-phase regions as isentropic, saturated mixtures. Both solved and non-condensable gas content is neglected in the model. Finally, viscous effects are neglected as well, assuming that the dynamics of cavitating flow are predominantly inertia-driven.

Hence, the governing equations are the unsteady, compressible Euler equations. Due to the barotropic assumption, the energy equation is not solved. Spatial discretization is performed on structured, body-fitted grids. Reconstruction of face velocities employs the non-linear limiter of Koren [10], an upwind reconstruction for the density and a 2^{nd}-order approximation for the pressure. Rotation is handled by an Arbitrary-Eulerian-Lagrangian (ALE) approach [11], applied to the complete domain. Explicit time integration is performed by a 4-stage Runge-Kutta method with a CFL-number of $CFL = 1.4$.

Thermodynamic properties of the fluid are computed by closed-form analytical relations. A modified Tait-equation [12] is utilized for computing the pressure $p(\rho)$ in the pure liquid. For water-vapor mixtures, p is obtained by integrating the equilibrium speed of sound $c^2 = \frac{\partial p}{\partial \rho}|_s$, taking the latent heat of vaporization into account [13]. The void fraction α can then be expressed using the mixture density ρ and the densities for the saturated liquid $\rho_{\mathrm{l,sat}}$ and vapor $\rho_{\mathrm{v,sat}}$ as $\alpha = (\rho - \rho_{\mathrm{l,sat}})/(\rho_{\mathrm{v,sat}} - \rho_{\mathrm{l,sat}})$. The saturation states of liquid and vapor are $p_{\mathrm{sat}} = 2339.3\,\mathrm{Pa}$, $\rho_{\mathrm{l,sat}} = 998.2\,\mathrm{kg/m^3}$ and $\rho_{\mathrm{v,sat}} = 0.0172\,\mathrm{kg/m^3}$, evaluated at the constant reference temperature $T_{\mathrm{ref}} = 20°\mathrm{C}$.

2.2 Assessment of Erosion Aggressiveness

Maximum Pressure Collapse events create pressure peaks, which can be utilized as a first measure of local flow aggressiveness. To this respect, the highest pressure encountered in each computational cell is recorded during the simulation. Pressure maxima on material walls allow to qualitatively identify erosion-sensitive areas.

The maximum pressure criterion, however, does not differentiate with respect to the origin of peak pressures. In addition to collapsing vapor structures, levels of increased pressure can also be caused by stagnation points or due to the superposition of pressure waves. The method furthermore emphasizes solely the strongest collapse events and does not e.g. provide information about the rate of occurrence.

Collapse Detection Algorithm The collective load of cavitating flow is composed of collapse events of different strengths and rates, which can be described by a load spectrum. Experiments indicate that these impact load spectra provide a more comprehensive quantification of cavitation aggressiveness [14, 15].

To this respect, we apply a *collapse detector*, developed by Mihatsch *et al.* [7], which enables the identification of isolated collapse events in space and time, including an estimation of the collapse strength. The implemented algorithm [7] first identifies isolated computational cells where complete condensation occurs. A collapse event is then characterized by a change of sign of local velocity divergence. The time, location, instantaneous collapse pressure and maximum condensation rate of thus detected events is recorded.

As shown by Schmidt *et al.* [6], maximum collapse pressures are resolution-dependent, i.e. peak pressures are inversely proportional to the cell size at the collapse center. This is reminiscent of the decay of a spherical, linear pressure wave with $p(r) \sim 1/r$. As discussed by Mihatsch *et al.* [7], this grid influence can be removed by introducing a reference length d_{ref} as a calibration parameter, as discussed below, and computing a "scaled collapse pressure" p_{scaled}:

$$p_{\mathrm{scaled}} \sim p_{\mathrm{collapse}} \cdot \sqrt[3]{V_{\mathrm{cell}}}/d_{\mathrm{ref}} \tag{1}$$

It is assumed that the focal point of the emitted pressure wave is equal to the center of the detected computation cell and that the radius of the initial wave front is proportional to $\sqrt[3]{V_{\mathrm{cell}}}$, i.e. the equivalent cell length based on the cell volume V_{cell}.

In addition to its influence on the peak pressure, the spatial resolution also dictates the scale of the smallest spatial structures that can be represented on a given mesh. An increasing number of smaller vapor structures is generated on finer grid levels. As each vapor structure potentially can cause a collapse, the rate of collapse events N is also resolution-dependent. Thus, a scaling law for obtaining a scaled collapse rate N_{scaled} is proposed by Mihatsch *et al.* [7]. For the present study, it has been adapted as follows:

$$N_{\mathrm{scaled}} \sim N \cdot \chi^{\kappa} \quad , \qquad \text{with} \quad \chi = d_{\mathrm{grid}}/d_{\mathrm{ref}} \tag{2}$$

Mihatsch *et al.* [7] utilizes the equivalent cell length $d_{\mathrm{grid}} = \sqrt[3]{V_{\mathrm{cell}}}$ to compute an individual length ratio χ for each collapse event. For the present inhomogeneous grid, however, it is more suitable to compute χ utilizing a mean grid length $d_{\mathrm{grid}} = \left\langle \sqrt[3]{V_{\mathrm{cell}}} \right\rangle$. The averaging has been performed within the vicinity of the blade where the majority of collapses occur. The value of d_{grid} is characteristic for each grid level, as shown in Tab. 1.

Based on experiments of cavitating flow within a radial divergent gap by Franc [15], Mihatsch *et al.* [7] calibrated d_{ref} and κ in Eqns. (1) – (2), yielding $d_{\mathrm{ref}} = 181\mu\mathrm{m}$, $\kappa = 3/2$. It is to be conjectured that these parameters are case-dependent, although this is still subject for investigation. In order to obtain a calibration for this study, it is necessary to quantify the impact load spectrum of the present propeller flow experimentally, which has not been conducted, yet. Since these scalings are mandatory when comparing results from different grid levels, the cited values for d_{ref} and κ are adopted here as well. Consequently, Eqns. (1) – (2) in this context do not provide absolute values for the collapse rates and pressures levels, that can be compared, e.g., to the material yield strength.

3 TEST CASE

Model Propeller VP1304 For the present study, experiments by the Schiffbau-Versuchsanstalt (SVA) Potsdam involving the five-bladed model propeller *VP1304* are reproduced numerically. In the context of the Potsdam Propeller Test Case (PPTC), a large body of data, comprised of both experimental work as well as numerical studies, has been published [16, 17]. The *VP1304* has a diameter of $D = 250\,\mathrm{mm}$, a chord length at $r/R = 0.75$ of $c_{0.75} = 106.3\,\mathrm{mm}$ and a root chord length of $c_{0.3} = 45.0\,\mathrm{mm}$. With the present study, we focus on PPTC operating condition *2.3.1*, characterized by the non-dimensional advance coefficient $J_{\mathrm{ref}} = V_a/nD = 1.019$, based on the advance velocity $V_a = 6.37\,\mathrm{m/s}$ and rate of revolution $n = 24.987\,\mathrm{rev/s}$. The cavitation number is $\sigma_n = (p_{\mathrm{amb}} - p_{\mathrm{vap}})/(1/2\,\rho_{\mathrm{ref}}\,(nD)^2) = 2.024$, with the ambient pressure $p_{\mathrm{amb}} = 42.3\,\mathrm{kPa}$, the vapor pressure $p_{\mathrm{vap}} = 2.82\,\mathrm{kPa}$ and reference density $\rho_{\mathrm{ref}} = 997\,\mathrm{kg/m^3}$.

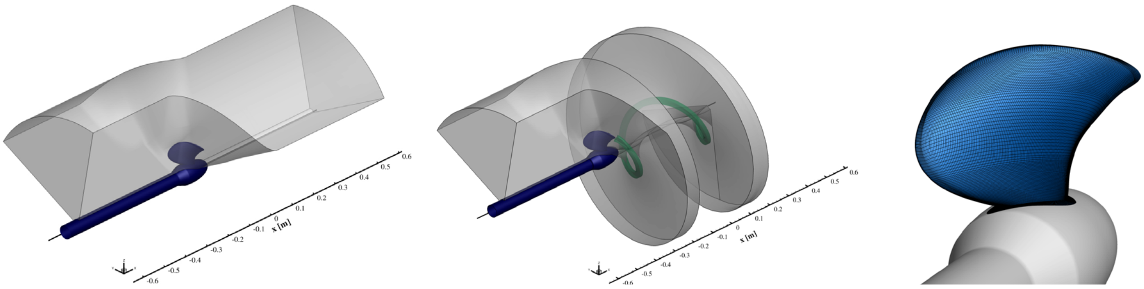

(a) *reference* configuration (straight propeller wake region)

(b) *tipvortex* configuration, (helix within propeller wake, with refined region highlighted)

(c) Blade surface mesh (*fine* grid).

Figure 1: Computational domains utilized in this study

Computational Domain All simulations are performed on a 72° blade passage. The utilized computational domains are shown in Figs. 1a and 1b. The *reference* configuration, Fig. 1a, is oriented axially within the propeller wake region. Preliminary studies showed that for properly capturing the cavitating trailing tip vortex, high spatial resolution is necessary. Thus, the *tipvortex* configuration describes a helix within the propeller wake, as shown by Fig. 1b. Based on the *reference* domain, the pitch angle of the helix $\Theta(x)$ has been adjusted *a priori* to follow the trailing tip vortex structure. By aligning a refined grid region, as highlighted in Fig. 1b, with the vortex core, the spatial resolution of this structure can be increased within the structured grid topology.

The influence of spatial resolution is investigated by a grid study. In the following, results from the *coarse*, *medium* and *fine* grids of the *tipvortex* configuration are discussed and compared to the *fine* level of the *reference* configuration. The latter does not include a refined tip vortex area. The characteristics of the numerical grids, together with the analysis intervals used for data collection, are summarized in Tab. 1. A visualization of the discretized blade surface on the *fine tipvortex* mesh is given in Fig. 1c. The blade resolution for this grid level, in terms of an average cell edge length in surface tangential and normal direction, is $l_{\mathrm{tan}} = 1$ mm and $l_{\mathrm{norm}} = 0.5$ mm, respectively.

Table 1: Properties of the utilized grid levels

level	no. of cells	min. cell size	d_{grid}	avg. timestep	analysis interval
coarse (tv.)^a	$1.2 \cdot 10^5$	0.5 mm	2.11 mm	$4.6 \cdot 10^{-8}$ s	18.07 rev
medium (tv.)^a	$6.6 \cdot 10^5$	0.2 mm	1.25 mm	$2.2 \cdot 10^{-8}$ s	21.98 rev
fine (tv.)^a	$5.2 \cdot 10^6$	0.1 mm	0.63 mm	$6.4 \cdot 10^{-9}$ s	3.35 rev
fine (ref.)^b	$3.4 \cdot 10^6$	0.1 mm	0.65 mm	$6.9 \cdot 10^{-9}$ s	2.87 rev

^{a} *tipvortex* configuration , ^{b} *reference* configuration

Boundary Conditions Inlet, outlet and radial boundaries are located at $l = 2D$ away from the propeller. Sponge layers ensure that wave reflections from the interior of the domain are reduced. At the inlet, the inflow velocity v_{in} is prescribed, controlling the effective advance coefficient $J = v_{\mathrm{in}}/nD$. For the outlet, a pressure boundary condition is employed, in order to obtain σ_n-similarity. At circumferential boundaries periodicity is enforced, while radial boundaries and material surfaces are modeled as slip-walls.

The PPTC problem statement requires thrust identity under wetted conditions. Thus, v_{in} is adapted, in order for the thrust coefficient $K_{\mathrm{T}} = T/\rho_{\mathrm{ref}}\, n^2 D^4$ to agree with the reference value $K_{\mathrm{T}}^{\mathrm{ref}} = 0.387$ obtained in the experiments. As described by Budich *et al.* [9], the effective advance coefficient J was increased by 6.5% with respect to J_{ref}, for realizing a thrust coefficient $K_{\mathrm{T}} = 0.389$, deviating less than 0.5% from the reference.

4 RESULTS AND DISCUSSION

Overview A snapshot of the instantaneous flow field on the *fine tipvortex* grid is given in Fig. 2. Cavitating structures are visualized by iso-surfaces of 10% void fraction, while iso-surfaces of vorticity magnitude $|\nabla \times \mathbf{u}| = |\boldsymbol{\omega}| = 1000\,\mathrm{s}^{-1}$ highlight vortical structures. In addition, $|\boldsymbol{\omega}|$ is also shown on a plane within the propeller wake. At the selected operating point, the flow is characterized by a highly unsteady suction side root cavitation. Exhibiting a periodic shedding-type behavior, vapor pockets are repeatedly generated along the root span. Under the influence of the adverse pressure gradient, these cavities collapse in the aft-part and close to the blade trailing edge. Suction side root cavitation is connected to the production of vortical structures close to the propeller axis. Moreover, a tip vortex develops above $r/R \gtrsim 0.95$ along the tip, and stays correlated over several diameters behind the propeller. The tip vortex core starts to cavitate along the blade surface. Further downstream, a cavitating trailing portion of this vortex extends beyond the blade into the propeller wake for the *tipvortex* domain, owing to the increased spatial resolution of this configuration. This is, in contrast, not observed on the *reference* domain.

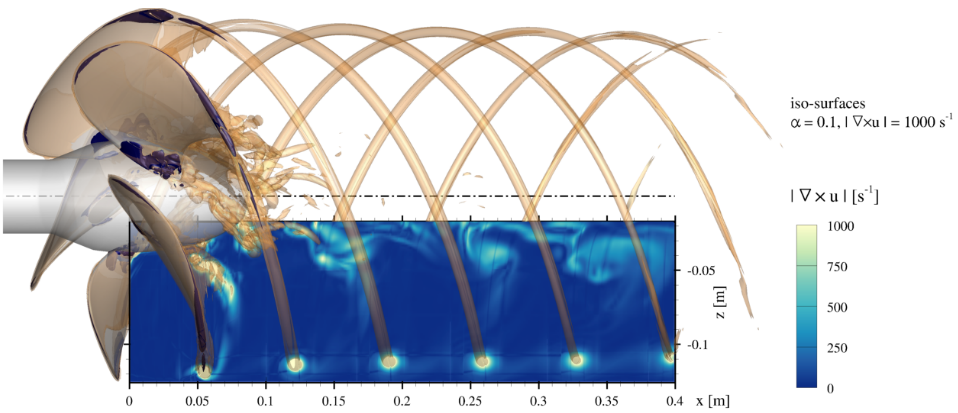

Figure 2: Visualization of instantaneous propeller flow by means of iso-surfaces of void fraction $\alpha = 0.1$ (blue) and vorticity magnitude $|\boldsymbol{\omega}| = 1000\,\mathrm{s}^{-1}$ (orange), as well as $|\boldsymbol{\omega}|$ on a plane within the propeller wake flow (*fine* mesh, *tipvortex* configuration)

The cavitating tip vortex is relatively stable and does not shed, which is in agreement to the experimental references [16]. In the experiments, however, the trailing vortex cavitates over a longer distance, while simulations yield re-condensation after about one 95%-blade chord length $c_{0.95}$. Further downstream of this location, axial grid spacing increases again. Although the vortex itself remains correlated over a large distance, this underlines the necessity of high spatial resolution for properly resolving a cavitating trailing tip vortex.

Validation As demonstrated by Budich *et al.* [9], the proposed method is in very good agreement with experimental as well as numerical references published within the PPTC [17]. The chosen inviscid approach, as expected, overestimates the wetted propeller performance η_0. However, with a deviation of $\lesssim 3\%$, the present simulation is still in an acceptable range in the context of the PPTC. Furthermore, cavitation extent in the vicinity of the blade is slightly overestimated. A similar tendency of over-prediction was also observed for the PPTC [17]. While leading edge cavitation was observed for most PPTC studies, it is almost absent from present results, which is in agreement with the experiments [16]. Further comparison with LDV measurements within the propeller wake showed, that propeller wake flow is reproduced accurately on planes $x/D = 0.1$ and $x/D = 0.2$ [9]. In particular, utilizing the *tipvortex* domain, the trailing tip vortex structure is well captured. Moreover, the pressure distribution on the blade surface has been validated against numerical studies involved in the PPTC [17] and agreement again is satisfactory.

Qualitative Erosion Assessment Qualitative evaluation of flow aggressiveness is given by Fig. 3. The maximum instantaneous pressures on material walls, recorded on the *fine tipvortex* domain, are shown in Fig. 3a. Collapse events, registered during the same time span, are summarized in Fig. 3b. Each detected event is represented by a circle, colored and scaled by the corresponding collapse pressure p_{collapse}.

The maximum pressure criterion shows a zone of increased pressure in the rear part of the suction side root area, where shed vapor structures collapse. Due to the short simulation time, distinctive footprints from individual collapse events can be identified. Almost all high-intensity pressure levels are located below $r/R = 0.45$ and downstream of 70% root chord length. Highest wall pressures exceed 130 bar in this area.

No traces of high pressure are present around the blade tip, as the cavitating tip vortex is relatively stable near the blade. This is also confirmed by Fig. 3b: The cavitating tip vortex causes collapse events only at the location of re-condensation, away from the blade.

The scatter plot furthermore shows a dense accumulation of events within and downstream of the suction side root area. A better assessment of these events is possible from Figs. 4a – 4d. Here, only collapses exceeding a threshold pressure $p_{\text{collapse}} > p_{\text{th}}$ with $p_{\text{th}} = \{10, 20, 40, 80\}$ bar are shown. Most weak events occur within 30%-60% of the root chord length and are excluded in these plots. As expected, the strongest collapse events are concentrated around the trailing edge.

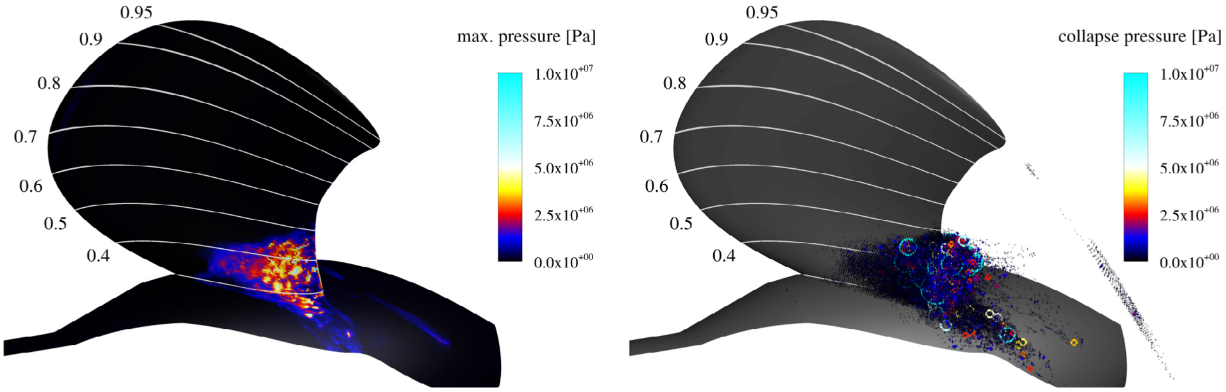

(a) Maximum pressure recorded on material walls (b) Detected collapse events

Figure 3: Maximum pressure criterion and detected collapse events, as recorded during the complete analysis interval (*fine* mesh, *tipvortex* configuration)

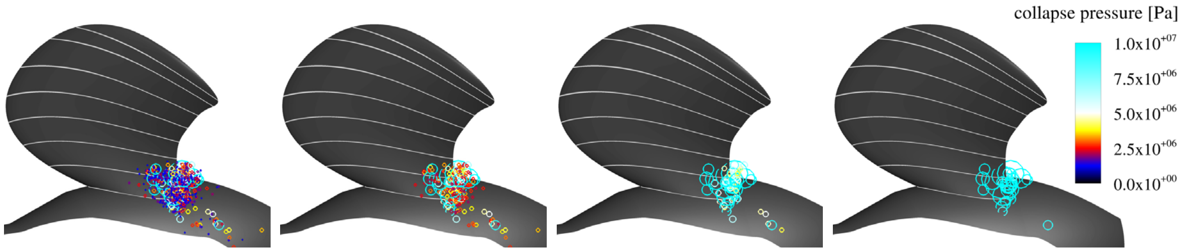

(a) $p_{\mathrm{th}} = 10\,\mathrm{bar}$ (b) $p_{\mathrm{th}} = 20\,\mathrm{bar}$ (c) $p_{\mathrm{th}} = 40\,\mathrm{bar}$ (d) $p_{\mathrm{th}} = 80\,\mathrm{bar}$

Figure 4: Detected collapse events with $p_{\mathrm{collapse}} > p_{\mathrm{th}}$ (*fine* mesh, *tipvortex* configuration)

Cavity Dynamics In Fig. 5a, the time signal of the non-dimensional thrust coefficient K_{T} is compared to the total vapor volume V_{vap}. The latter is computed by integrating α within the complete domain $V_{\mathrm{vap}} = \int_V \alpha \, dV$. Both quantities show a fluctuating behavior, which is dominated by the shedding process of the suction side root cavitation. This shedding can be characterized by a dominant frequency $f_{\mathrm{cav}} \approx 137.6\,\mathrm{Hz}$, as shown by a Fourier analysis [9]. It is concluded in [9], that cavity dynamics lead to an excitation of the propeller, that is close, but not equal, to the blade passing frequency (BPF). In addition, superimposed on the fluctuating time signals of the thrust coefficient in Fig. 5a are peaks due to stochastically occurring cavity collapse events in the vicinity of the blade. In the corresponding power spectra [9], this causes broad band noise at higher frequencies.

Collapse events can be linked to the global vapor condensation rate $-\dot{V}_{\mathrm{vap}} = -\partial V_{\mathrm{vap}}/\partial t$. The time signal of $-\dot{V}_{\mathrm{vap}}$ is compared in Fig. 5b to the instantaneous maximum collapse strength $\max(p_{\mathrm{collapse}})$ and the instantaneous collapse rate N_{collapse}. Highest collapse rates are encountered during time segments when condensation outweighs vapor production, i.e. $-\dot{V}_{\mathrm{vap}} > 0$. In general, these phases are also associated with the occurrence of the strongest collapse events. Deviations can occur as this analysis compares *global* quantities, e.g. not taking into account balancing effect of simultaneous production and condensation of vapor structures in different regions of the flow.

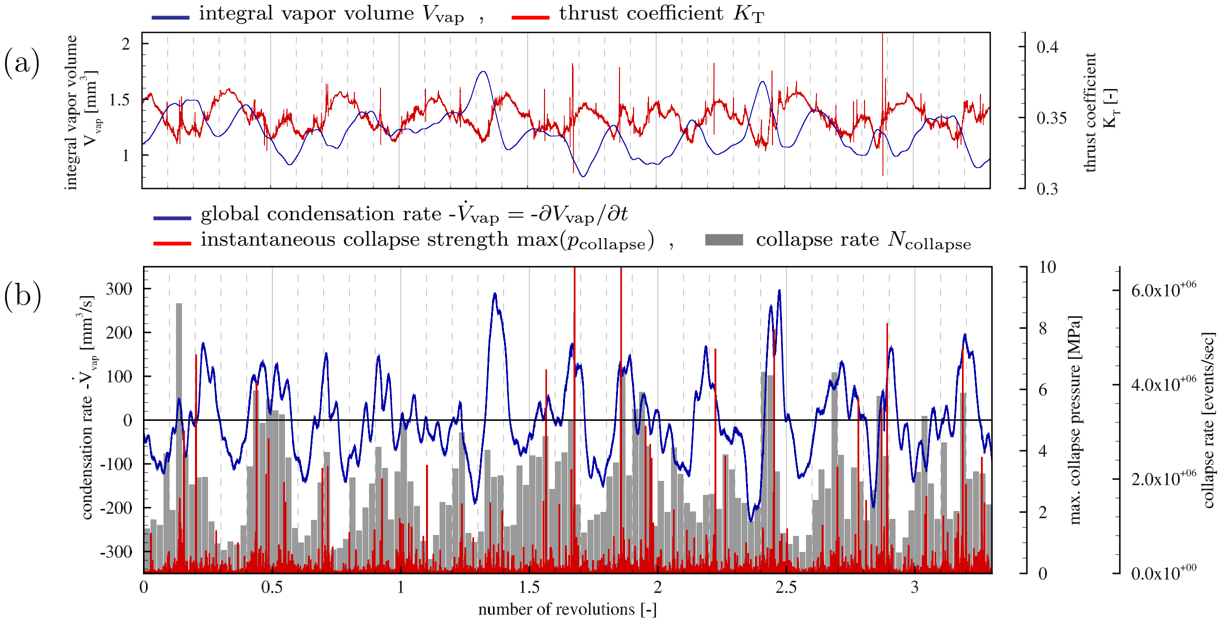

Figure 5: Time evolution of collapse-related quantities (*fine* mesh, *tipvortex* configuration)

Global Collapse Load Spectra The cumulative load spectra of recorded collapse events are shown in Fig. 6. The analysis is conducted for all four grids within the complete computational domain. Pressure levels that have been reached less than 10 times have been excluded, which applies to the highest collapse pressures. The strongest collapse, which occurred on the *fine* grid of the *reference* domain yields $p_{\text{collapse}} = 173\,\text{bar}$.

In Fig. 6a, the unscaled pressure p_{collapse} is plotted. Despite different refinement levels for the tip vortex, the *fine reference* and *fine tipvortex* grid agree. Comparing the different spatial resolutions, a grid dependence can be observed, yielding higher-intensity collapses on finer grid levels, as explained above. Excluding the weakest pressure levels, the obtained collapse rates N follow an exponential behavior $N \sim a\exp(\text{-}b\,p)$ with constants a, b, as indicated by trendlines. This is characteristic for various properties quantifying cavitation intensity [18], such as pressure peaks or pitting rates [15, 19].

The application of the pressure scaling, Eq. (1), is displayed in Fig. 6b. The slopes for the *fine* and *medium* grid are nearly identical, with a constant offset between the two levels. Application of Eq. (2) corrects the offset between the *medium* and *fine* grid levels, see Fig. 6c, corroborating the suitability of the proposed pressure and rate scalings.

In contrast, the slope for the *coarse* mesh deviates from the *medium* and *fine* levels in Figs. 6b and 6c. A visual inspection of the transient flow on the *coarse* grid level shows that shedding is observed only in the rear part of the suction side root, with an attached portion close to the leading edge. For the *medium* and *fine* levels, however, the root cavitation periodically separates along the complete chord. It is thus concluded that the coarse resolution is insufficient for resolving enough relevant flow scales in order to exhibit shedding dynamics analogous to the finer levels.

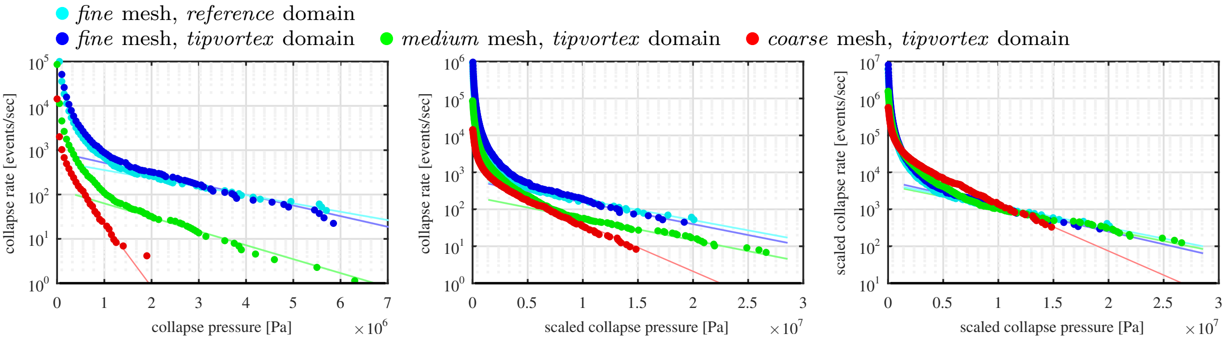

(a) Collapse rate N vs. collapse pressure p_{collapse}

(b) Collapse rate N vs. scaled collapse pressure p_{scaled}

(c) Scaled collapse rate N_{scaled} vs. scaled collapse pressure p_{scaled}

Figure 6: Cumulative collapse spectra of collapse events detected within the complete domain (global spectra), comparison of all four grid configurations (events occurring <10 times excluded)

Local Collapse Load Spectra Local flow aggressiveness can be further analyzed by classifying collapses by their location. For two criteria, this is shown in Figs. 7a and 7b.

In Fig. 7a, collapses are classified according to their distance d to the nearest material wall, utilizing bins of $\Delta d = 1$ mm up to a maximum distance of $d_{\max} = 10$ mm. For medium-intensity collapses, the highest rates are registered directly at the wall, i.e. within a distance of $0 \leq d \leq 2$ mm. However, the highest collapse strength does not occur near the wall but at a distance of $2-3$ mm. Note that the near wall region is highly under-resolved due to the Euler grid. Therefore, the method does not contain microscopic scales, such as the formation of micro-jets directed towards the wall, collapses of micro cavities or cavitating turbulent eddies. Instead, only larger vapor structures are sufficiently resolved.

Fig. 7b categorizes collapses by their streamwise position along the root chord. Control planes separating the bins are placed perpendicular to the direction of relative flow along the blade root chord length $c_{0.3}$, spanning from the leading edge (0%), to the trailing edge (100%) and extending into the propeller wake up to $2 \cdot c_{0.3}$ (200%). The histogram shows that flow aggressiveness is maximal at the trailing edge (80-100%) and directly downstream (100-120%).

5 CONCLUSIONS

With the present study, a fully compressible simulation is applied to the cavitating model propeller *VP1304*. Under the assumptions of thermodynamic equilibrium and barotropic flow, a density-based numerical approach, combined with a homogeneous mixture model is utilized. This method enables the resolution of the coupled behavior of phase transition and wave dynamics. While suitability of the adopted method and validation was demonstrated in a previous paper [9], the current contribution focuses on an assessment of flow aggressiveness. Two criteria are utilized: recorded maximum pressures and a numerical prediction of collapse load spectra. To this respect, collapse rates and strengths of individual collapse events are recorded with the *collapse detector* algorithm.

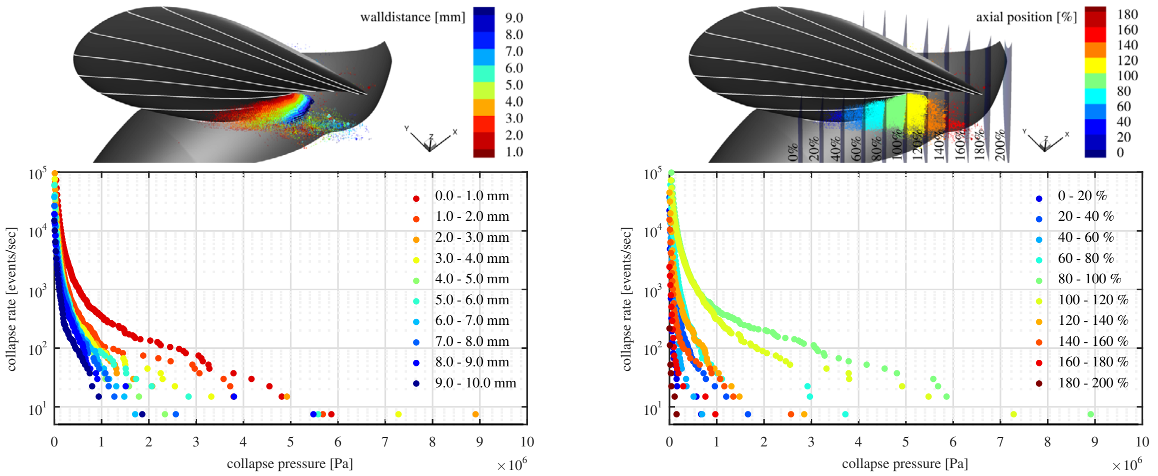

(a) Categorized by distance to the nearest material wall d (up to $d_{\max} = 10\,\mathrm{mm}$)

(b) Categorized by stream-wise position along blade root chord (control planes as shown)

Figure 7: Cumulative collapse spectra of collapse events detected within certain regions (local spectra), results of the *fine* mesh, *tipvortex* configuration (all collapses shown)

For the chosen operating point, cavitation is observed in the core of the tip vortex and in the suction side root region. The stable tip vortex causes only weak collapse events in the area of recondensation, downstream of the propeller. Consequently, no traces of increased wall pressure are observed on the blade itself. In contrast, the suction side root cavity repeatedly generates vapor pockets that collapse in the vicinity of the blade. Cavitation dynamics excite instantaneous pressure loads on the structure, stemming from the shedding mechanism as well as from individual collapse events. Both collapse rates and collapse strengths are connected to the global rate of condensation -$\dot{V}_{\mathrm{vap}}$.

Global collapse spectra exhibit an exponential relation between cumulative collapse rates and collapse strengths. This is commonly found for the intensity of cavitating flow undergoing a shedding-like behavior. A grid study shows the resolution-dependence of the load spectrum. The proposed pressure and rate scalings, adapted from [7], can be used to remove this grid influence, provided that the relevant flow dynamics are captured. Consequently, results for the *medium* and *fine* grid levels yield identical collapse spectra.

Highest maximum pressures are encountered in the rear part of the blade and directly on the trailing edge. Accordingly, the most aggressive local collapse spectra are found in this region. Furthermore, local collapse spectra utilizing the wall distance of the registered events are presented. Highest collapse rates are found directly at the wall, while the most violent events are located in a distance of $2-3\,\mathrm{mm}$ away from the blade.

In addition to the presented analyses, investigations of the PPTC operating points *2.3.2* and *2.3.3* are currently realized. This allows to investigate different flow regimes such as pressure-side cavitation. Additionally, a comparison of flow aggressiveness for different flow conditions can be conducted. Finally, the spatial resolution is further refined in order to perform a more detailed analysis of the cavitating tip vortex structure.

ACKNOWLEDGMENTS

Support for this research was provided by the U.S. Office of Naval Research (ONR) and ONR Global through the NICOP entitled “Numerical Investigation of Ship-Propeller Cavitation with Full Description of Shock-Wave Dynamics” (Contract No. N62909-12-1-7034). The authors are grateful for Dr. Ki-Han Kim (ONR HQs) and Dr. Woei-Min Lin (ONR Global) for their support and guidance throughout this project. The authors further acknowledge the Gauss Centre for Supercomputing e.V. (www.gausscentre.eu) for providing computing time on the GCS Supercomputer *SuperMUC* at the Leibniz Supercomputing Centre (LRZ, www.lrz.de).

REFERENCES

[1] Terwisga, T. J. C. van, Wijngaarden, E. van, Bosschers, J., and Kuiper, G. “Achievements and challenges in cavitation research on ship propellers”. *International Shipbuilding Progress*, Vol. 54(2), 2007, pp. 165–187.

[2] Carlton, J. S. *Marine Propellers and Propulsion.* Third Edition. 2012, Butterworth-Heinemann, Oxford.

[3] Philipp, A. and Lauterborn, W. “Cavitation erosion by single laser-produced bubbles”. *Journal of Fluid Mechanics*, Vol. 361, 1998, pp. 75–116.

[4] Schnerr, G. H., Sezal, I. H., and Schmidt, S. J. “Numerical investigation of three-dimensional cloud cavitation with special emphasis on collapse induced shock dynamics”. *Physics of Fluids*, Vol. 20(4), 2008, pp. 040703–040703–9.

[5] Schmidt, S. J., Thalhamer, M., and Schnerr, G. H. “Inertia controlled instability and small scale structures of sheet and cloud cavitation”. *Proc. of the 7th International Symposium on Cavitation.* Ann Arbor, Michigan, USA, Aug. 2009.

[6] Schmidt, S. J., Mihatsch, M. S., Thalhamer, M., and Adams, N. A. “Assessment of the Prediction Capability of a Thermodynamic Cavitation Model for the Collapse Characteristics of a Vapor-Bubble Cloud”. *Proc. of the 3rd Warwick International Cavitation Forum.* Warwick, UK, July 2011.

[7] Mihatsch, M. S., Schmidt, S. J., Thalhamer, M., and Adams, N. A. “Quantitative Prediction of Erosion Aggressiveness through Numerical Simulation of 3-D Unsteady Cavitating Flows”. *Proc. of the 8th International Symposium on Cavitation 2012.* Singapore, Aug. 2012.

[8] Mihatsch, M. S., Schmidt, S. J., and Adams, N. A. “Cavitation Erosion Prediction based on Analysis of Flow Dynamics and Impact Load Spectra”. 2015. Submitted for publication in *Physics of Fluids.*

[9] Budich, B., Schmidt, S. J., and Adams, N. A. "Numerical Investigation of a Cavitating Model Propeller Including Compressible Shock Wave Dynamics". *Proc. of the 4th International Symposium on Marine Propulsors.* June 2015. Accepted.

[10] Koren, B. "A robust upwind discretisation method for advection, diffusion and source terms." *Numerical Methods for Advection-Diffusion Problems.* Ed. by Vreugdenhil, C. B. and Koren, B. 1993. Chap. 5, pp. 117–138.

[11] Donea, J., Huerta, A., Ponthot, J., and Rodríguez-Ferran, A. "Arbitrary Lagrangian-Eulerian methods". *Encyclopedia of Computational Mechanics.* Ed. by Stein, E., Borst, R. de, and Hughes, T. J. R. 2004, John Wiley & Sons. Chap. 14, pp. 413–437.

[12] Sezal, I. H. "Compressible Dynamics of Cavitating 3-D Multi-Phase Flows". PhD thesis. Technische Universität München, 2009.

[13] Franc, J.-P. and Michel, J.-M. *Fundamentals of Cavitation.* Ed. by Moreau, R. 2004, Kluwer Academic Publishers.

[14] Fortes-Patella, R., Reboud, J.-L., and Archer, A. "Cavitation damage measurement by 3D laser profilometry". *Wear*, Vol. 246(1-2), 2000, pp. 59–67.

[15] Franc, J.-P. "Incubation Time and Cavitation Erosion Rate of Work-Hardening Materials". *Journal of Fluids Engineering*, Vol. 131(2), 2009, pp. 021303–021303–14.

[16] SVA Potsdam GmbH. *Potsdam Propeller Test Case (PPTC) - Cavitation Tests with the Model Propeller VP1304, Report 3753.* Technical Report. Apr. 2011.

[17] Hoekstra, M., Terwisga, T. J. C. van, Heinke, H.-J., Lübke, L., Abdel-Maksoud, M., and Druckenbrod, M., eds. *Proceedings of SMP'11 Workshop on Cavitation and Propeller Performance: the Second International Symposium on Marine Propulsors.* 17 – 18 June, 2011, Hamburg, Germany.

[18] Knapp, R. T. "Recent investigations of the mechanics of cavitation and cavitation damage". *Transactions of the ASME*, Vol. 77, 1955, pp. 1045–1054.

[19] Franc, J.-P., Riondet, M., Karimi, A., and Chahine, G. L. "Impact Load Measurements in an Erosive Cavitating Flow". *Journal of Fluids Engineering*, Vol. 133(12), 2011, pp. 121301–121301–8.